Supplementary Information

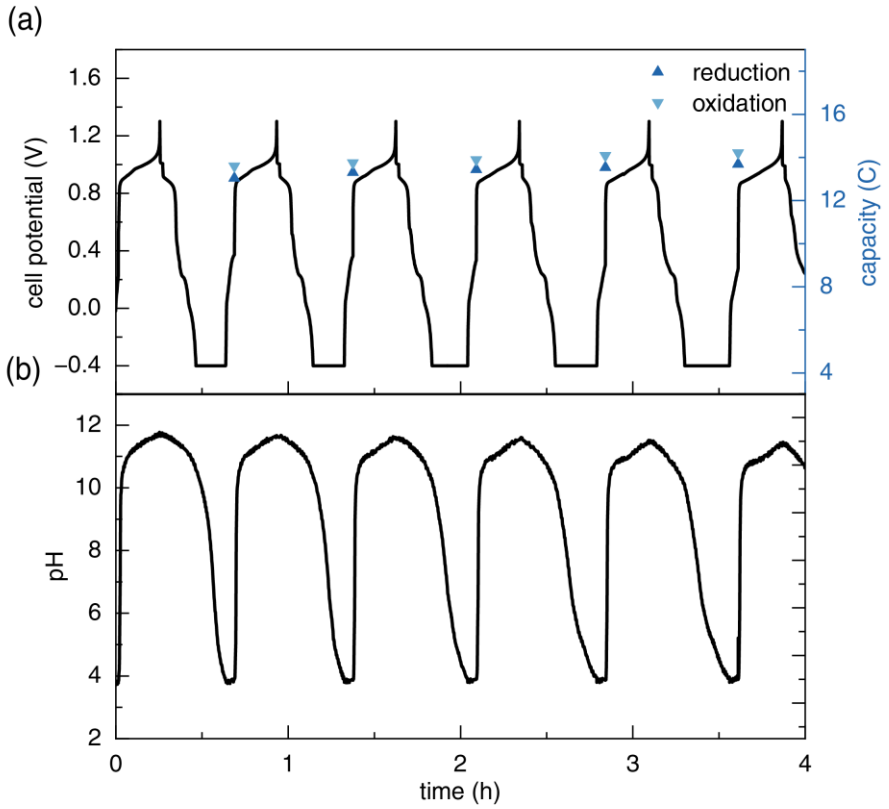

Supplementary Fig.1. Cell cycling in 1 M KCl (10 mL, DI water) using a phenazine–carbon nanotube electrode drop-cast on graphite felt, with a non-capacity-limiting counter electrolyte comprising 30 mM $K_3Fe(CN)_6$/$K_4Fe(CN)_6$ (40 mL). (a) Cell potential and capacity during cycling with constant-current charge and discharge at 3 mA cm^{-2}, with a constant-voltage step applied during discharge only at −0.4 V until the current decayed to 0.4 mA cm^{-2} to enforce a reversible pH swing and enable ≈ 100% Coulombic efficiency. (b) Corresponding bulk pH evolution during repeated cycles.

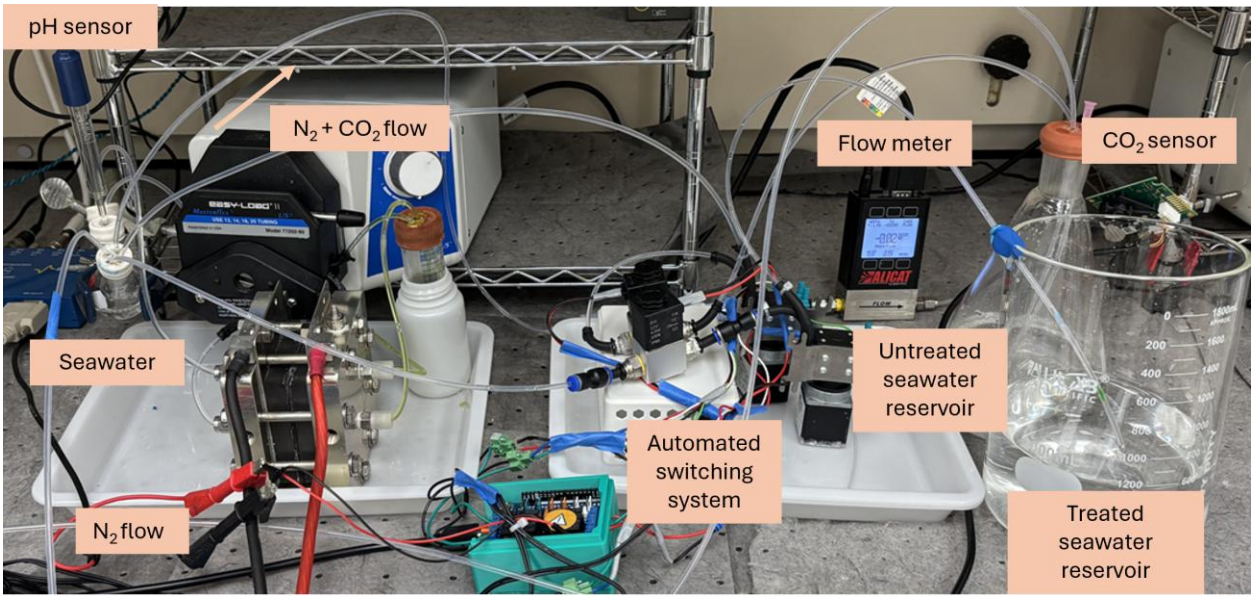

Supplementary Fig.2. Semi-continuous CO_2 removal setup with automated seawater delivery. Photograph of the electrochemical flow-cell system coupled to an automated switching module that alternates between untreated and treated seawater reservoirs. Controlled N_2 and N_2/CO_2 gas streams, along with inline pH and CO_2 sensors, enable semi-continuous cycling and monitoring during operation.

Supplementary Note 1

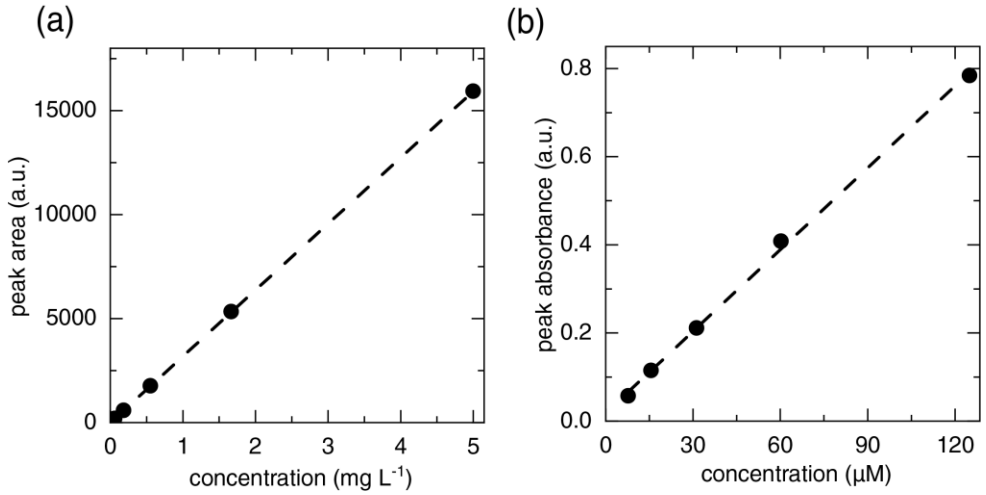

Supplementary Fig.3. Calibration curves for phenazine quantification. (a) HPLC calibration curve showing integrated peak area (a.u.) as a function of phenazine concentration (mg L^{-1}) measured by diode array detection at 362 nm. (b) UV–Vis calibration curve showing peak absorbance (a.u.) as a function of phenazine concentration (μM) measured at 364 nm. Dashed lines indicate linear least-squares fits.

A UV–Vis calibration curve for phenazine was constructed using standards prepared in a matrix of 90% synthetic seawater and 10% ethanol. Absorbance spectra were recorded at 364 nm. Linear regression yielded the calibration relationship $y = 0.0108 + 0.00619x$, where y is the peak

absorbance (a.u.) and x is the phenazine concentration (μM), with a coefficient of determination $R^2 = 0.999$ (Supplementary Fig.3a). Treated seawater samples, diluted to 90% sample and 10% ethanol, exhibited a peak absorbance of 0.064 at 364 nm. Ocean Optics DH-2000-BAL light source coupled to an Ocean HDX spectrometer for this process. All UV–Vis measurements were performed using an Ocean Optics DH-2000-BAL light source coupled to an Ocean HDX spectrometer.

Phenazine was quantified by high-performance liquid chromatography (HPLC, 1260 Infinity II, Agilent Technologies, USA) using an XDB-C18 column (4.6 mm × 250 mm, 5 μm). The mobile phase consisted of 60% phosphoric acid (0.1% in water) and 40% acetonitrile at a flow rate of 1 mL min^{-1} with a 100 μL injection volume, and detection was performed at 362 nm using a diode array detector (DAD). An external calibration curve was constructed by plotting integrated peak area as a function of phenazine concentration. Linear regression yielded the calibration relationship $y = -5.33 + 3187.49x$, where y is the integrated peak area (a.u.) and x is the phenazine concentration (mg L^{-1}), with a coefficient of determination $R^2 \approx 0.999$ (Supplementary Fig.3b). Treated seawater samples analyzed under identical conditions exhibited an integrated peak area of 4342.2 and were quantified using this calibration.

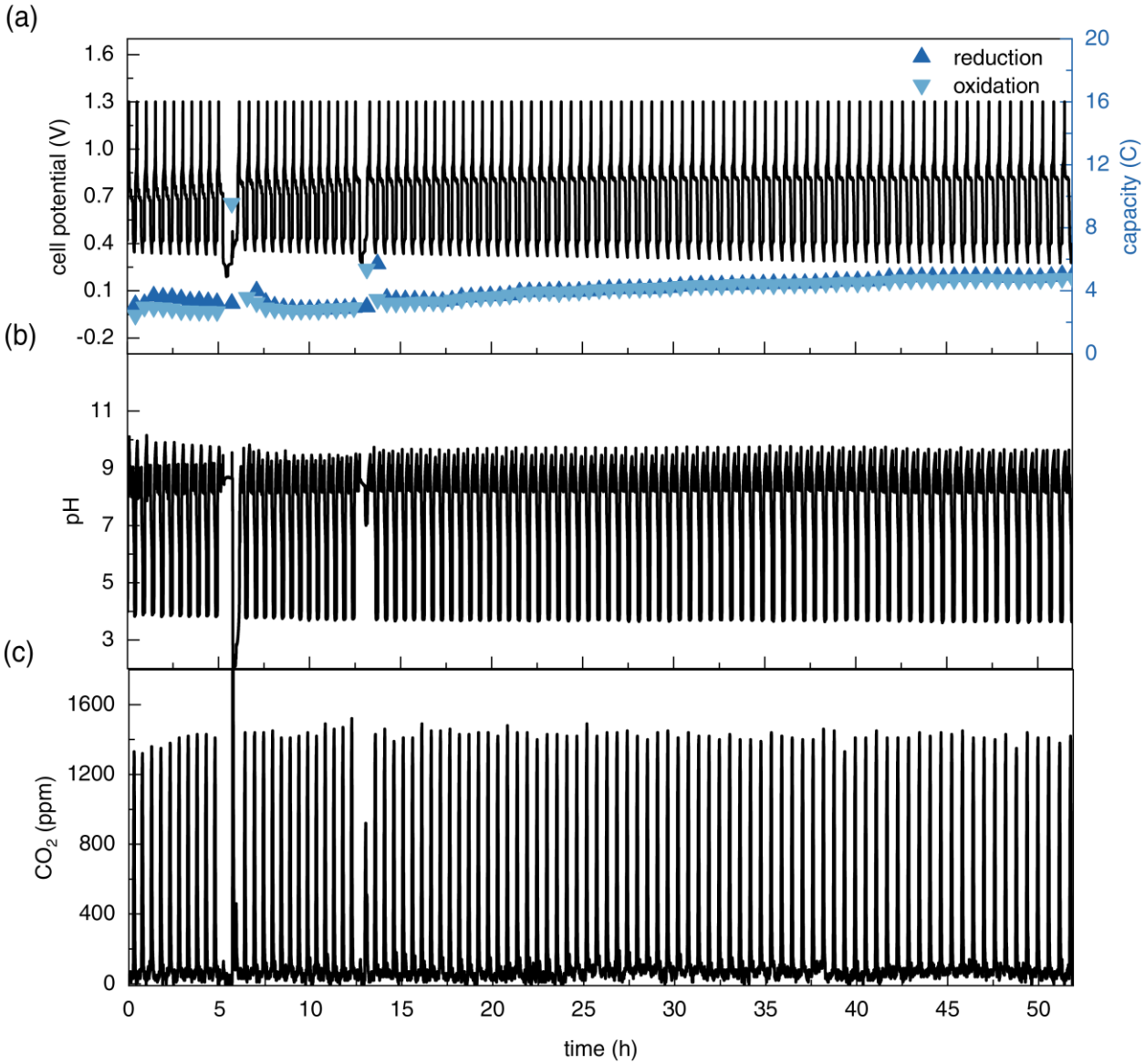

Supplementary Fig.4. (a) Cell voltage during cycling of 10 mL real seawater (per cycle) in the negative electrolyte and 30 mM $Na_4Fe(CN)_6/Na_3Fe(CN)_6$ (30 mL) as the posolyte, recorded at 2 mA cm^{-2} with a charging cutoff of 1.3 V and a discharging cutoff at seawater pH 4. (b) Seawater pH over time. (c) CO_2 concentration (ppm) over time. Seawater was collected from a coastal site in the Long Island Sound region (41°19′24.1″ N, 71°59′08.7″ W) and filtered through a 0.22 µm membrane to remove suspended particulates and microorganisms prior to electrochemical experiments. Four cycles (cycles 16–17 and 30–31) were excluded from analysis due to missed electrolyte refilling events associated with intermittent trigger signal detection.

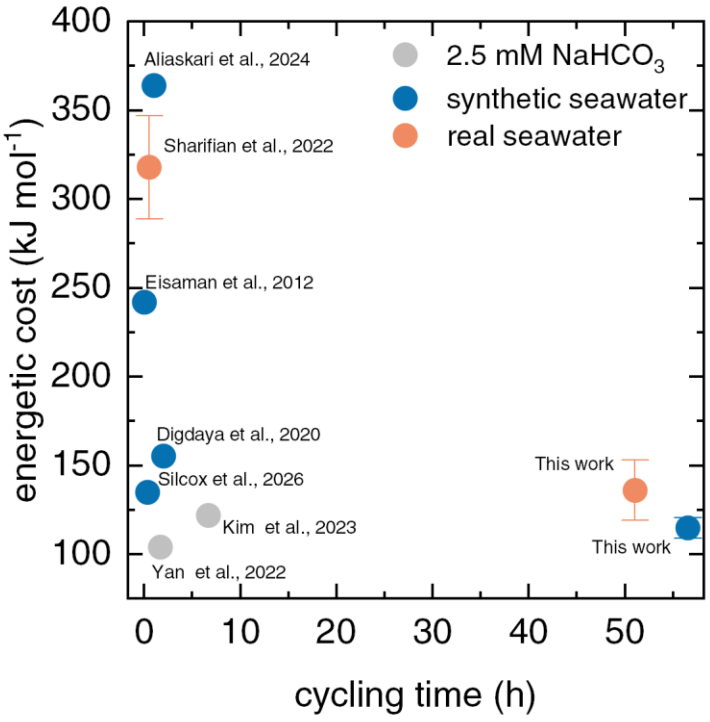

Supplementary Fig.5. Total cycling time versus energetic cost (kJ mol^{-1} CO_2) for this work and prior studies.[1-7] Blue markers denote synthetic seawater systems, gray markers indicate bicarbonate electrolytes (2.5 mM $NaHCO_3$), and orange markers represent real seawater.

Supplementary Note 2

Reaction-Transport Model of PCET-driven CO_2 Separation

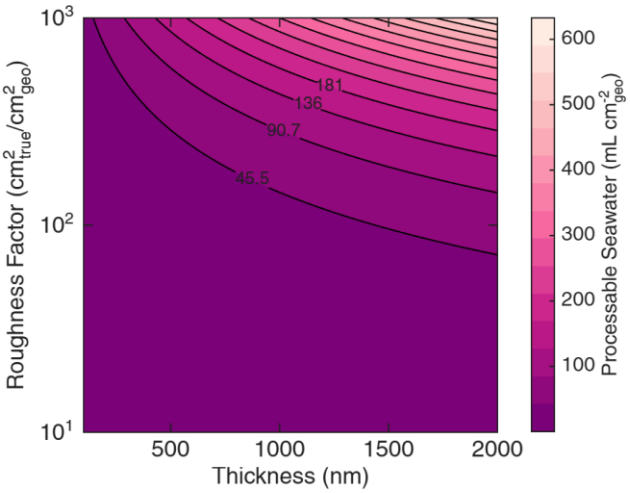

Supplementary Fig.6. Dependence of processable seawater volume on the PCET-active film thickness and roughness factor (RF), assuming a charge of 244 C L^{-1} fully converts bicarbonate and carbonate species to CO_2(aq).

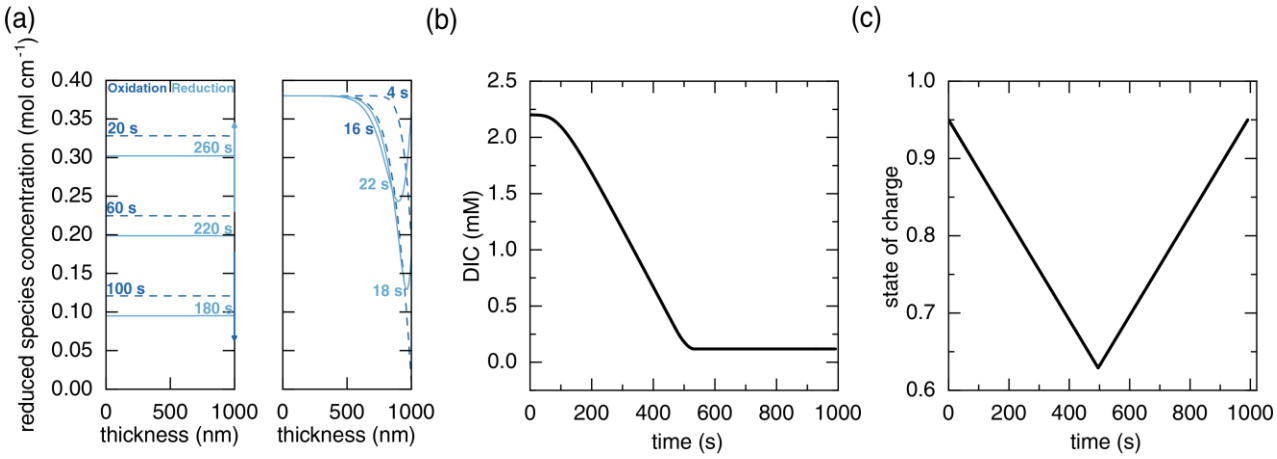

Supplementary Fig.7. (a) Simulated concentration profiles of reduced PCET species during electrode oxidation and reduction at 10 mA cm^{-2}_{geo}, comparing proton diffusivities (D_H) of 10^{-7} and 10^{-11} cm^2 s^{-1} with 0.4 mol cm^{-1} active species loading. Model-predicted cycling behavior of a PCET electrode operated at 1 mA cm^{-2}_{geo} for (b) DIC concentration (mM) and (c) SOC at the electrode-seawater interface.

The modeling domain comprises a redox-active film of thickness d_a subdivided into a grid of 100 equally spaced points. The last (rightmost) index of the grid ($x = d_a$) is the interface between the PCET-active electrode film and the seawater solution whereas the first (leftmost) index ($x = 0$) corresponds to the film|current collector interface. We chose 100 grid points based on a grid independence check, to ensure result stability while minimizing computational cost.

Areal loading of the PCET-active electrode

The density of PCET-active moieties within the film (in mol cm^{-3}) is the following function of areal loading in terms of true surface area (AL_{true}, in $mol_{phenazine}$ cm^{-2}_{true}) and d_a:

$$PCET\ density = \frac{AL_{true}}{d_a} \tag{S1}$$

This PCET density depends on the molecular mass and structure of the active PCET species and on the film-formation process (e.g., drop-casting, solution processing, or in situ polymer growth), which together determine the resulting electrode morphology.[8,9] Bulk densities of such films are rarely reported; typical dense organic polymers fall within 0.9–1.3 g cm^{-3},[10] so we adopt 0.88 g cm^{-3} as a representative lower-bound value for a compact active layer. At this density, the attainable concentration of redox units within a film is approximately ≈ 4 × 10^{-3} mol cm^{-3}. This

assumption provides a consistent basis for comparing diverse PCET-active material systems. Based on a film thickness of 1 μm, we calculate a theoretical AL_{true} of 4×10^{-7} mol cm^{-2}_{true}. The areal loading in terms of geometric (projected) area, (AL_{geo}, in $mol_{phenazine}$ cm^{-2}_{geo}) is the product of AL_{true} and the roughness factor (RF, in cm^2_{true}/cm^2_{geo}), which we define as the ratio of true to geometric (projected) surface area.

The one-dimensional concentration of PCET centers in the film (C_T) depends on the product of AL_{true}, RF, and geometric electrode area, A_{geo}:

$$C_T = \frac{AL_{true} \times RF \times A_{geo}}{d_a} \quad \text{(S2)}$$

Reported roughness factors for carbon electrodes span approximately RF ≈ 1–200, depending on morphology and accessible surface area.[11-18] For our model, we adopt RF = 20 as a conservative baseline within this range. For A_{geo} = 5 cm^2 and RF = 20, the one-dimensional concentration of redox-active sites is $C_T \approx 0.4$ mol cm^{-1}.

We assume that each redox site undergoes a $2e^-$, $2H^+$ PCET and that a charge of 244 C L^{-1} is sufficient to fully convert bicarbonate and carbonate species to CO_2(aq).[23] On this basis, the maximum processable seawater volume per geometric area is shown in Supplementary Fig.6 as a function of d_a and RF. For d_a = 1 μm, this corresponds to seawater-to-area ratios of approximately 0.32–64 mL cm^{-2}_{geo} across RF = 1–200. Methods based on templating, nano-structuring, and hierarchical growth can yield roughness factors well above the range considered here,[19] indicating opportunities for substantially increasing accessible surface area in future PCET-active electrodes.

Electron-coupled proton diffusion within the PCET-film

The formation of and interconversion between reduced protonated species (RH_2) and oxidized species (O) within the film occurs through electron-coupled proton hopping between adjacent sites, expressed using the one-dimensional diffusion equation:

$$\frac{\partial C_{RH2}}{\partial t} = D_H \frac{\partial^2 C_{RH2}}{\partial x^2} \quad \text{(S3)}$$

where D_H is the effective proton diffusivity within the film and is a function of the rate of electron self-exchange (k_{ex}) according to $D_H = k_{ex}\delta^2 C/6$, where C and δ are the redox site concentration and nearest-neighbor hopping distance, respectively.[20]

Conversion between O and RH_2 occurs at the interface between the film and seawater according to:

$$D_H \frac{\partial C_{RH2}}{\partial x} = \frac{i}{nF} \, at \; x = d_a \tag{S4}$$

where the applied current i is positive for reduction of O to RH_2. We impose a no-flux boundary condition at the film|current collector interface:

$$D_H \frac{\partial C_{RH}}{\partial x} = 0 \; at \; x = 0 \tag{S5}$$

The concentration of oxidized species, C_O, is computed through mass balance:

$$C_O = C_T - C_{RH2} \tag{S6}$$

We assume electron-coupled proton diffusion within the film that is rate-limited by an effective proton diffusivity.[21] Estimates for D_H in proton-conducting redox-active materials vary widely depending on the material and measurement technique. In hydrogenated metal oxides, reported D_H values vary between ≈ 10^{-5} and 10^{-16} cm^2 s^{-1}.[22] In redox-active quinone polymers, values as low as ≈ 10^{-11} – 10^{-12} cm^2 s^{-1} have been reported.[20,23-25] However, other quinone-based polymers have shown exceptional rate capability and low activation barriers for proton transport (< 300 meV) when deployed as aqueous battery materials, suggestive of the presence of hydrogen-bonding networks for rapid proton conduction through a Grotthuss-type mechanism.[26-28] We therefore assume a baseline D_H of 10^{-7} cm^2 s^{-1} as representative of the highest achievable D_H, but also report simulations in which D_H is 10^{-11} cm^2 s^{-1}, in recognition of values commonly reported in the literature (Supplementary Fig.7a).

Cell potential

The pH-dependent half-cell potential is calculated as follows:

$$E_{total} = E_{OCV} + \Delta E_{Activation} + \Delta E_{Ohmic} \tag{S7}$$

$$E_{OCV} = \frac{RT}{nF} ln\left(\frac{C_O}{C_{RH2}}\right) - 0.059 \frac{mV}{pH} \times pH_{seawater} \tag{S8}$$

$$\Delta E_{Activation} = \frac{RT}{\alpha nF} asinh\left(\frac{j}{2j_0}\right) \tag{S9}$$

$$\Delta E_{Ohmic} = R_{Ohmic} jA \tag{S10}$$

where $\Delta E_{activation}$ is the activation overpotential, ΔE_{Ohmic} represents an Ohmic overpotential (due to cell resistance), R is the universal gas constant (8.314 J mol^{-1} K^{-1}), T is temperature (25 °C), n is the number of electrons transferred per PCET center (2), j_0 is the exchange current density in mA

cm^{-2}_{true}, R_{Ohmic} is the cell resistance (assumed to be 5 Ω cm^2), α is the transfer coefficient, and j is the applied current density in mA cm^{-2}_{true}.

The current density j and exchange current density j_0 are defined as follows:

$$\frac{j}{FA_{true}} = k_s\left(\sqrt{\Gamma_O}e^{-\alpha\frac{F}{RT}(\Delta E_{Activation})} - \sqrt{\Gamma_{RH2}}e^{(1-\alpha)\frac{F}{RT}(\Delta E_{Activation})}\right) \quad \text{(S11)}$$

where A_{true} is the true surface area, and Γ is the surface molar concentration at the film|seawater interface in mol cm^{-2}_{true}.

The exchange current density is defined for $j = 0$[29]:

$$\frac{j_0}{A_{true}} = Fk_s{\Gamma_O}^{(1-\alpha)}{\Gamma_{RH}}^{\alpha} \quad \text{(S12)}$$

where k_s is the interfacial electron-transfer rate constant (s^{-1}).

We parameterized the pH dependence of k_s using a two-branch acid/base PCET model[30]:

$$k_s(\text{pH}) = k_a^0 10^{-(1-\alpha_a)\,\text{pH}} + k_b^0 10^{\alpha_b(\text{pH}-pK_w)} \quad \text{(S13)}$$

with pK_w =14.00 at 25 °C. The other parameters (k_a^0, α_a, k_b^0, α_b) were estimated from nonlinear least squares fitting of experimentally reported k_s values for self-assembled monolayers of hydroxy-anthraquinone between pH 2 and 14 (Table S1).[31] Equation (S13) was then used to dynamically update k_s as seawater pH evolved.

Table S1. Values of Fitted Coefficients

k_a^0	4.86 s^{-1}
α_a	0.73
k_b^0	209.7 s^{-1}
α_b	1.57

Combining Eqs. (S11) and (S12) yields:

$$j = j_0\left(e^{-\alpha F\Delta E_{Activation}/RT} - e^{(1-\alpha)F\Delta E_{Activation}/RT}\right) \quad \text{(S14)}$$

Under the assumption that α = 0.5, this expression can be rearranged to obtain Eq. (S9).

DIC speciation and removal

The total alkalinity (TA) of seawater can be expressed as follows[32]:

$$\frac{10^{-14}M^2}{[H^+]} + \frac{DIC}{1 + \frac{[H^+]}{K_1} + \frac{K_2}{[H^+]}} + 2\frac{DIC}{1 + \frac{[H^+]}{K_2} + \frac{[H^+]^2}{K_1K_2}} - [H^+] \quad \text{(S15)}$$

where the contribution from borate species is ignored.

The rate of change of TA is directly proportional to the applied current *i*:

$$\frac{dTA}{dt} = -\frac{i}{FV_{seawater}} \quad \text{(S16)}$$

Dissolved inorganic carbon (DIC) is defined as follows:

$$DIC = [CO_2(aq)] + [HCO_3{}^-(aq)] + \left[CO_3{}^{2-}(aq)\right] \quad \text{(S17)}$$

DIC is removed from seawater at a rate proportional to $[CO_2(aq)]$ and a rate constant for CO_2 removal, k_L:

$$\frac{dDIC}{dt} = -k_L([CO_2(aq) - CO_2(eq)]) \quad \text{(S18)}$$

where $[CO_2(eq)] = K_H\, p_{CO_2}$. K_H is the Henry's law constant for CO_2 dissolution (3.0×10^{-2}mol $L^{-1}\ atm^{-1}$), and we take $p_{CO_2} = 4.2 \times 10^{-4}$ atm.

The rate constant k_L was estimated using technical data sheets for a 3M liquid–gas membrane contactor (Liqui-Cel-EXF-10x28) and direct correspondence with the supplier. Based on fluid residence times and CO_2 removal efficiencies, we estimate a k_L on the order of ≈ 0.1 s^{-1}. This estimate, however, corresponds to single-pass CO_2 removal. In the present configuration, where seawater is continuously circulated through a reservoir with fluid volume V_r at a flow rate F_v, the effective rate constant for CO_2 removal (k_L') is a function of V_r, F and the CO_2 removal fraction η according to $k_L' = \eta F_v/V_r$. For example, assuming V_r = 10 mL, F = 40 mL min^{-1}, and η = 0.75 results in k_L' = 0.05 s^{-1}.

The following reactions determine the pH-dependent distribution of DIC species:

$$CO_2(aq) + H_2O \overset{K_1}{\rightleftharpoons} HCO_3^-(aq) + H^+(aq) \overset{K_2}{\rightleftharpoons} CO_3^{2-}(aq) + 2H^+(aq) \quad \text{(S19)}$$

where activity-corrected first and second dissociation constants for carbonic acid (K_1 and K_2) are $10^{-5.86}$ M and $10^{-8.92}$ M, respectively.[33]

Given any two among TA, DIC and pH, the third can be calculated. We therefore initialize the seawater system using pH = 8.1 and DIC = 2.2 mM, which are typical for seawater, resulting in an initial TA = 2.4 mM. These values are close to those for the synthetic seawater (DIC ≈ 2.11 mM, TA ≈ 2.28 mM) and real seawater (DIC ≈ 1.87 mM, TA ≈ 2.04 mM) used in this study, where TA was measured and DIC was calculated as described in the Methods section. After each timestep, TA and DIC are re-evaluated using equations (S16) and (S18), respectively, after which pH is computed using equation (S15). The equations were solved using a nonlinear equation solver in Python.[34] In cases where the solver gives a negative value for TA (for instance, due to numerical stiffness at low $[H^+]$), we redefine TA in terms of $[OH^-]$:

$$TA = [OH^-] + \frac{DIC}{1 + \frac{10^{-14}M^2}{K_1[OH^-]} + \frac{K_2[OH^-]}{10^{-14}M^2}} + 2\frac{DIC}{1 + \frac{10^{-14}M^2}{K_2[OH^-]} + \frac{(10^{-14}M^2)^2}{K_1K_2[OH^-]^2}} - \frac{10^{-14}M^2}{[OH^-]} \quad \text{(S20)}$$

$$[H^+][OH^-] = 10^{-14}M^2 \quad \text{(S21)}$$

We calculate the concentrations of the components of DIC assuming internal equilibrium among CO_2(aq), bicarbonate and carbonate:

$$[CO_2(aq)] = \frac{DIC}{1 + \frac{K_1}{[H^+]} + \frac{K_1K_2}{[H^+]^2}} \quad \text{(S22)}$$

$$[HCO_3^-] = \frac{DIC}{1 + \frac{[H^+]}{K_1} + \frac{K_2}{[H^+]}} \quad \text{(S23)}$$

$$[CO_3^{2-}] = \frac{DIC}{1 + \frac{[H^+]}{K_2} + \frac{[H^+]^2}{K_1K_2}} \quad \text{(S24)}$$

We assume internal equilibrium among DIC constituents because the conversion of HCO_3^- to CO_2(aq) under acidic conditions is much faster than CO_2 removal. At pH 5, the effective first-order rate constant for bicarbonate conversion to CO_2(aq) is $k_{eff} \approx 0.4$ s^{-1}, and it increases to $k_{eff} \approx 4$ s^{-1} at pH 4, as described by:

$$CO_2(aq) + H_2O \underset{k_{-1}}{\overset{k_{+1}}{\Leftrightarrow}} HCO_3^- + H^+ \quad \text{(S25)}$$

$$r_b = k_{-1}[H^+][HCO_3^-] = k_{eff}[HCO_3^-] \quad \text{(S26)}$$

where k_{-1} is 2.67×10^4 M^{-1} s^{-1}.[32]

Thus, around pH 4 – 5, the kinetics of CO_2 evolution exceed CO_2 removal, which occurs at a rate constant of $\approx 10^{-2}$ s^{-1}. As CO_2 removal is the overall rate-limiting step, carbonate speciation is assumed to remain at equilibrium.

Table S2. Representative parameters used in reaction–transport modeling of pH-swing CO_2 removal.

Description	**Value**	**Units**
PCET-active film thickness	1.0×10^{-4}	cm
Number of spatial grid points	100	–
Geometric electrode area	5	cm^2
Roughness factor	20	–
Film density	0.88	$g\cdot cm^{-3}$
Proton diffusivity	1.0×10^{-7}	$cm^2\cdot s^{-1}$
Faraday constant	96485	$C\cdot mol^{-1}$
Applied current density	1.0×10^{-3}	$A\cdot cm^{-2}$
Time step	0.1	s
Series resistance	4.0	Ω cm^2
Butler–Volmer symmetry factor	0.5	–
Initial dissolved inorganic carbon	2.2×10^{-3}	M
Initial proton concentration (pH ≈ 8.1)	7.94×10^{-9}	M
Water autoionization constant (pK_w)	14.0	–
CO_2 stripping rate constant	0.02	s^{-1}
Henry's law constant for CO_2	3.0×10^{-2}	$mol\cdot L^{-1}\cdot atm^{-1}$
Atmospheric CO_2 partial pressure	4.20×10^{-4}	atm

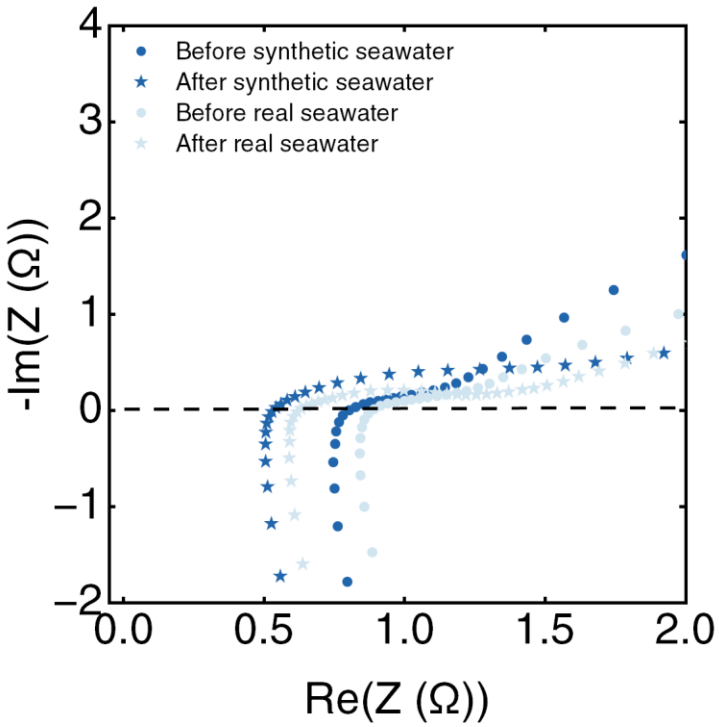

Supplementary Fig.8. Nyquist plots from electrochemical impedance spectra of flow cells containing the phenazine–carbon nanotube electrode measured before cycling and after cycling in seawater.

Supplementary Note 3

Stepwise acid–base titrations of synthetic seawater

We conducted stepwise acid-base titrations of synthetic seawater and bicarbonate solutions to experimentally examine the effect of the order of acid-base addition on pH swings in seawater (Table S3). In Experiments 1, 2, and 3, a 10 mL sample of synthetic seawater (initial pH ≈ 8.1) was titrated with 50 µL of 0.5 M HCl and KOH, corresponding to the addition of the same equivalents of protons and hydroxide ions. After each titration, the solution was stirred for 20 minutes to allow equilibration and precipitation, with a flow of nitrogen in the electrolyte headspace to remove any dissolved CO_2. In Experiment 1, the acid was added before base, leading to release of all DIC before alkalization. In the absence of divalent cations and precipitation, the pH would be expected to reach > pH 11, as was observed for a control measurement with 2.5 mM of $NaHCO_3$ (Experiment 3). In contrast, seawater only reached pH 10.03 ± 0.01 after alkalization, indicating the process of brucite precipitation consumed OH^- and capped further pH increases. When base was added before acid (Experiment 3), both calcite and brucite precipitation led to a significant consumption of alkalinity, and subsequent addition of acid caused a net reduction in the alkalinity of seawater and thus acidification (pH 7.97 ± 0.07). These results confirm that the

order of acid-base addition strongly influences the net decrease in alkalinity due to precipitation, and that enacting acidification and DIC removal prior to alkalization —as shown in this work—is the preferred protocol.

Although the precipitation of brucite decreases seawater alkalinity, its release to the ocean (pH ≈ 8), where it would be undersaturated, would in practice cause it to dissolve over time. This process will restore the alkalinity lost during precipitation in the cell. Under such conditions, solid precipitation may fortuitously decrease the energetic cost of CO_2 removal without reducing seawater alkalinity.

Table S3. Stepwise titration of carbonate and synthetic seawater solutions.

Experiment #		Stage 1		Stage 2		Stage 3
1	10 ml, Seawater	pH 8.18 ± 0.03	50 µl of 0.5 M HCl Added	pH 3.88 ± 0.06	50 µl of 0.5 M KOH Added	pH 10.03 ± 0.01
2	10 ml, Seawater	pH 8.11 ± 0.05	50 µl of 0.5 M KOH Added	pH 9.98 ± 0.05	50 µl of 0.5 M HCl Added	pH 7.97 ± 0.07
3	10 ml, $NaHCO_3$	pH 8.81 ± 0.02	50 µl of 0.5 M HCl Added	pH 4.34 ± 0.02	50 µl of 0.5 M KOH Added	pH 11.14 ± 0.09

Impact of Solid Precipitation on Energy Input

Zhang et al. identified precipitation of solids containing divalent cations as a dominant pathway underlying unintended acidification of the ocean in electrochemical pH-mediated carbon capture.[35] Because Mg^{2+} is the most concentrated divalent cation in seawater (54.1 mM[35]), it plays the predominant role in hydroxide consumption and thus loss of alkalinity. To quantify this effect, we incorporated brucite precipitation kinetics into our reaction–transport model, thus enabling evaluation of the influence of precipitation on DIC, cell potential, and energy costs.

Brucite precipitation is governed by the following expressions:

$$IAP_{Mg(OH)_2} = [Mg^{2+}]\,[OH^-]^2 \quad \text{(S27)}$$

$$\Omega_{Mg(OH)_2} = \frac{IAP_{Mg(OH)_2}}{K_{sp,Mg(OH)_2}} \quad \text{(S28)}$$

$$R_{f,Mg(OH)_2} = k_{Mg(OH)_2}\left(\Omega_{Mg(OH)_2} - 1\right)^{n_{Mg(OH)_2}} \quad \text{(S29)}$$

where each equivalent of hydroxide consumed in precipitation reduces total alkalinity as defined by Eq. (S20). Here, $IAP_{Mg(OH)_2}$ is the ion activity product, $\Omega_{Mg(OH)_2}$ is the saturation index, and $K_{sp,Mg(OH)_2}$ is the solubility product of $Mg(OH)_2$. The term $k_{Mg(OH)_2}$ denotes the precipitation rate constant (M s^{-1}), $R_{f,Mg(OH)_2}$ is rate of $Mg(OH)_2$ precipitation (M s^{-1}), and $n_{Mg(OH)_2}$ is an empirical reaction order. When $\Omega_{Mg(OH)_2} > 1$, there is a thermodynamic driving force for brucite precipitation, whereas when $\Omega_{Mg(OH)_2} < 1$, brucite dissolution is favored. The solubility product of brucite ($K_{sp,\text{ brucite}} = 10^{-10.56}$) was adjusted to account for ion activities in seawater using a total activity coefficient for Mg^{2+} of $\gamma_T = 0.26$.[36]

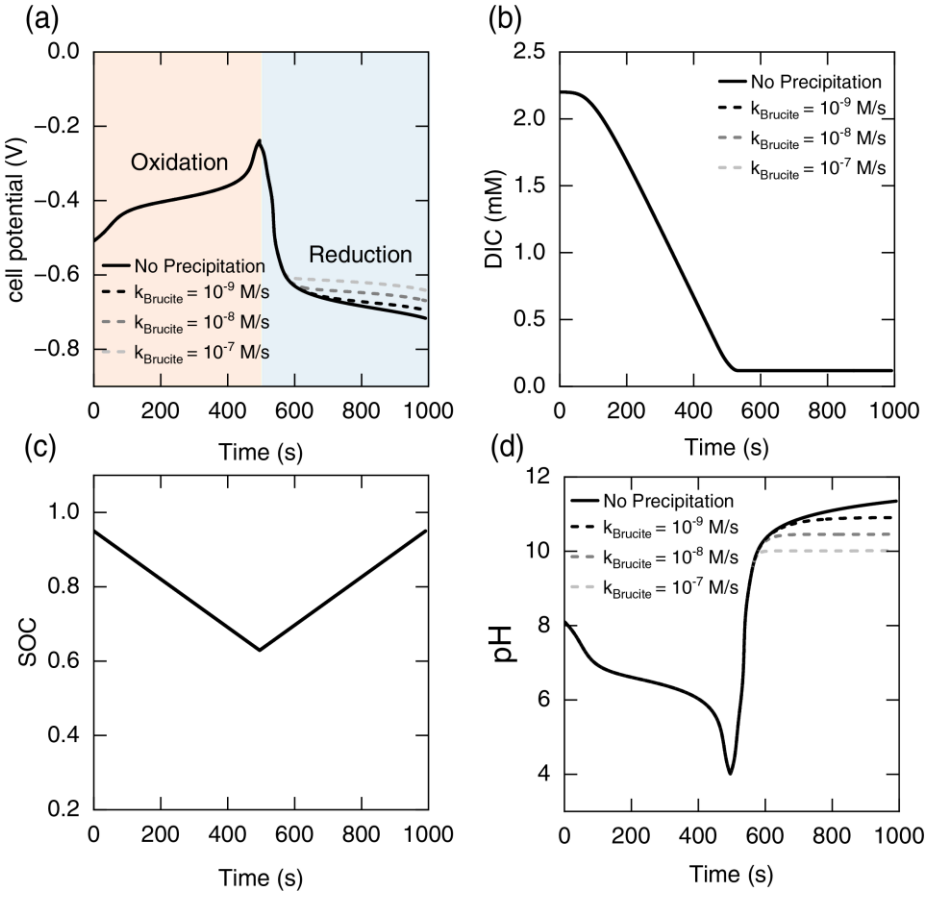

Supplementary Fig.9. Simulation results for one seawater CO_2 removal cycle at 1 mA cm^{-2}_{geo} incorporating brucite precipitation. Results compare a scenario with no precipitation (solid line) to precipitation at different kinetic rate constants ($k_{Mg(OH)_2}$= 10^{-9}, 10^{-8}, 10^{-7} M s^{-1}) under a fixed rate constant for CO_2 removal, k_L = 0.02 s^{-1}. Panels show (a) electrode potential, (b) dissolved inorganic carbon (DIC), (c) SOC at the film|seawater interface, and (d) seawater pH vs time.

There are significant uncertainties in the brucite precipitation rate constant. Zhang et al., suggest that brucite precipitation initiates near pH 9.1, and approaches completion between pH 10 and 14.

To account for this uncertainty, we explored a wide range of precipitation rate constants, from 0 (an infinitesimal rate of precipitation) to 10^{-7} M s^{-1}, the latter representing a regime in which precipitation above pH 10 reaches equilibrium virtually instantaneously. These assumptions enable evaluation of precipitation effects on system performance. We find that the energetic cost decreases slightly with increasing $k_{Mg(OH)_2}$ due to the lower final pH (as governed by (S8) and eq. 1), while the CO_2-depleted effluent remains alkaline (Supplementary Fig.9, Table S4).

Table S4. Effect of brucite precipitation kinetics on energetic cost and CO_2 separation rate with k_L=0.02 s^{-1}

$k_{Mg(OH)_2}$ (M s^{-1})	Energetic Cost (kJ mol^{-1} CO_2)	Separation Rate (µmol hr^{-1} cm^{-2}_{geo})
0	28.85	15.12
10^{-9}	27.79	15.12
10^{-8}	25.79	15.12
10^{-7}	23.22	15.12

While $CaCO_3$ precipitation represents an additional alkalinity-consuming pathway, we do not consider it here because carbonate activity will be too low for calcite formation following DIC removal during the acidification step.

Supplementary Note 4

Machine Learning and Global SHAP Analysis

Predictive design guidelines for electrochemical systems are inherently complex due to the nonlinear coupling between geometry, mass transport, electron transfer kinetics, and cost components—and their impacts across multiple spatial and temporal scales. To address this challenge in the context of our reaction-transport model for PCET-driven seawater carbon removal, we developed a two-stage, multi-output neural network model capable of learning a compact latent representation of four coupled system outputs (levelized cost, electrode utilization, energetic cost, and separation rate) and decoding them back into their physical and techno-economic units with high quantitative fidelity. This framework integrates large-scale sampling, rigorous dataset curation, variance-aware target encoding, principal-component regression, and game-theoretic explainability via SHaply Additive exPlanations (SHAP)[37] (see Supplementary Fig.10a). The resulting machine learning reproduces the reference electrochemical model across physical and cost domains while remaining interpretable in terms of chemically meaningful process variables. Machine learning was implemented in MATLAB 2025a using the *Statistics and Machine Learning Toolbox* and custom ensemble-training utilities optimized for high-dimensional, variance-stabilized regression. The input space comprised ten descriptors (see Table S5, and Supplementary Fig.10b). A Latin hypercube sampling (LHS) design was employed to generate a total of 1×10^7

data points, providing stratified coverage of the multidimensional parameter space defined by the ranges in Table S5. Parameter combinations yielding non-finite or physically implausible outputs were masked prior to training, with the feasible subset constrained to CO_2 separation cycles with energetic cost < 600 kJ mol^{-1} CO_2. All input features were normalized using Z-score standardization to enhance gradient conditioning, as their magnitudes spanned multiple orders of magnitude. The curated dataset was then randomly partitioned into 60% training, 20% validation, and 20% test subsets, yielding approximately 2.33×10^6, 7.77×10^5, and 7.77×10^5 physically valid samples per split after masking.

The regressor model consists of a two-stage neural network architecture. In the first stage, the four interdependent targets—energetic cost (kJ mol^{-1} CO_2), electrode utilization, levelized cost of CO_2 removal (\$ ton CO_2^{-1}), and separation rate (μmol hr^{-1} cm^{-2})— were transformed into a variance-stabilized latent space using logarithmic and logit mappings, followed by principal-component analysis (PCA) to decorrelate cross-target dependencies. In the second stage, an ensemble of fully connected neural networks was trained to predict the PCA scores. Each network consisted of five hidden layers with widths of 600, 450, 300, 150, and 75 neurons, each activated by rectified linear units (ReLU), and optimized using a mean-square-error loss function with early-stopping regularization. Model convergence was stable and repeatable across all folds. The corresponding validation mean absolute percentage errors (MAPE) were 3.42% (energetic cost), 4.77% (electrode utilization), 3.73% (levelized cost of CO_2 removal), and 3.25% (separation rate). This demonstrates very close quantitative agreement between predicted and reference values across both physical and techno-economic domains. The residual distributions were normal, homoscedastic, and unbiased, confirming the absence of systematic deviation and the high generalization integrity of the surrogate.

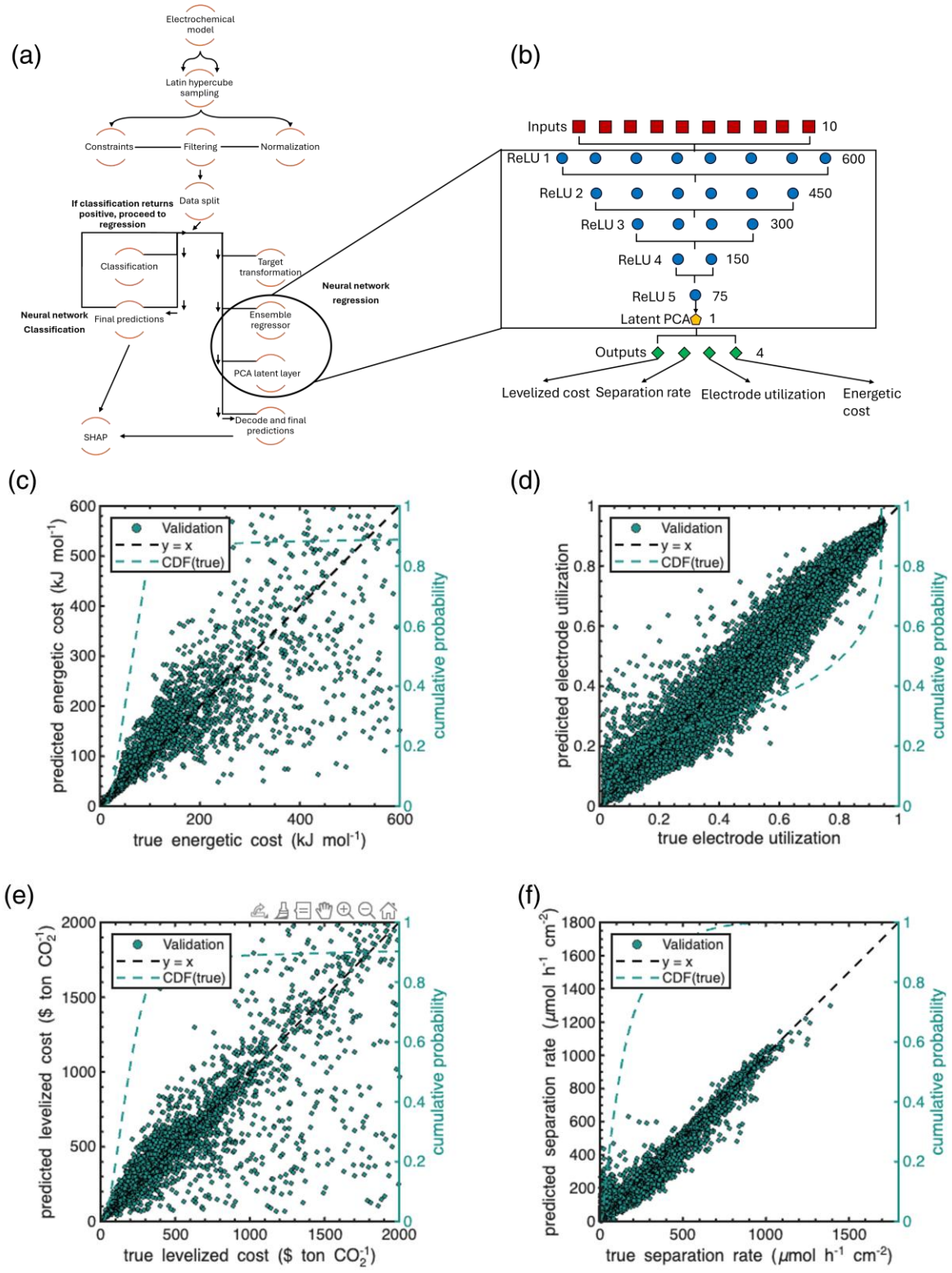

Supplementary Fig.10. Machine-learning framework and model performance. (a) Statistical training pipeline, beginning from previously described electrochemical model to classifier neural network and conditionally, the multioutput regression neural network. (b) Schematic of the more

complex regression neural network and eventual latent multioutput. (c-f) parity plots with residual distributions for the four targets (energetic cost = 0.96 R^2, electrode utilization = 0.99 R^2, levelized cost = 0.96 R^2, and separation rate = 0.98 R^2), for the validation dataset. ReLU denotes the rectified linear unit activation functions used in the hidden layers of the neural networks, and Latent PCA refers to the principal component analysis applied in the latent target space to decorrelate and compress the multioutput response before decoding back to the original physical quantities.

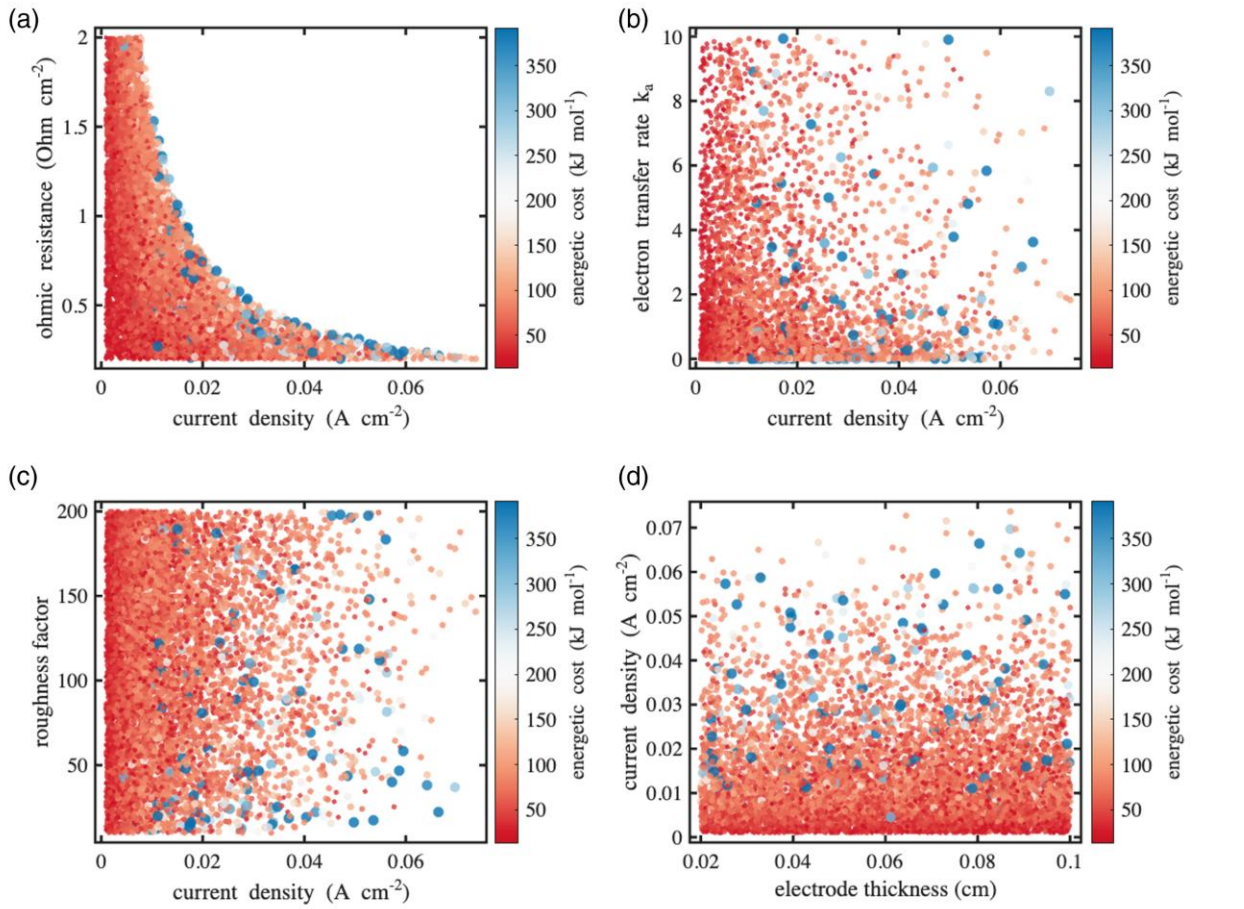

Supplementary Fig.11. Global neural-network energetic-cost maps. (a) Energetic cost (kJ mol^{-1} CO_2) as a function of Ohmic resistance (Ω cm^2) and current density (A cm^{-2}). (b) Energetic cost (kJ mol^{-1} CO_2) as a function of electron transfer rate constant and current density (A cm^{-2}). (c) Energetic cost (kJ mol^{-1} CO_2) as a function of roughness factor and current density (A cm^{-2}). (d) Energetic cost (kJ mol^{-1} CO_2) as a function of current density (A cm^{-2}) and PCET film thickness (cm). In all panels, energetic cost is predicted by the trained neural-network surrogate, with all non-plotted variables fixed at their median physical values; the color scale is truncated at 600 kJ mol^{-1} CO_2 for clarity.

Table S5. Electrochemical model parameters fed into the machine learning framework.

Parameter	**Range**	**Units**
Thickness	$2\times10^{-4} – 10\times10^{-4}$	cm
Current density	$1\times10^{-3} – 100\times10^{-3}$	A cm^{-2}
Roughness factor	10 – 200	–
Ohmic resistance	5 – 50	Ω cm^2
CO_2 removal rate constant	0.05 – 0.5	s^{-1}
Proton diffusivity	$1\times10^{-11} – 1\times10^{-6}$	cm^2 s^{-1}
Interest rate	0.02 – 0.12	–
Electricity price	0.01 – 0.5	\$ kWh^{-1}
k_a	$1\times10^{-4} – 10$	s^{-1}
k_b	$1\times10^{-2} – 1\times10^{3}$	s^{-1}

Supplementary Note 5

Techno-Economic Analysis

Baseline Assumptions

Table S6 presents techno-economic parameters related to financing, replacement of capital equipment, and the energetics of CO_2 removal using vacuum stripping across a gas-exchange hollow-fiber membrane. For this analysis, we assume an effective CO_2 removal rate constant of 0.02 s^{-1}, a conservative lower-bound value drawn from the range of k_L estimates derived in the *DIC speciation and removal* section. This choice reflects uncertainties in membrane-contactor performance, particularly under scaled operating conditions. These values are held fixed in the subsequent analysis.

Table S6. Parameters for techno-economic analysis

Parameter	**Value**

Separation rate	100,000	$ton_{CO2}\ yr^{-1}$
Energy penalty - vacuum pump CO_2 stripping	0.059	$kWh\ kg_{CO2}^{-1}$
Energy penalty - vacuum pump pre-degasification O_2/N_2	0.014	$kWh\ kg_{CO2}^{-1}$
Energy penalty - cooling	0.002	$kWh\ kg_{CO2}^{-1}$
Cost of Commercial Electricity ($ kWh^{-1})	0.03	$ kWh^{-1}
Cost Factor for Cell Components	1.4	
Capacity Factor (CF)	0.9	
Interest rate for discounting	0.065	

Capital and Material Costs

The entire system consists of cell stack components (cation-exchange membrane, carbon electrode), balance-of-plant equipment (membrane contactor, water condenser, vacuum pump, and chiller), and electrode/active materials (phenazine, carbon nanotubes or activated carbon, PFSA binder, and $Na_4Fe(CN)_6$). The components are limited to only those essential to system performance, providing a simplified configuration that establishes a baseline for cost.

Table S7 outlines the specific costs of the counter electrolyte chemical sodium ferrocyanide ($Na_4[Fe(CN)_6]$) and the materials required for the PCET electrode fabrication. We selected $Na_4Fe(CN)_6$ over $K_4Fe(CN)_6$ due to the former's lower cost, and because Na^+ is the most abundant cation in seawater.[38] We assumed a lifetime of 2 years for both the counter electrolyte and all PCET electrode components.

Because no reliable bulk market price for phenazine is publicly available, we assume a phenazine price of \$10 kg^{-1}, in keeping with the current assumptions in the TEA literature for organic flow batteries, where phenazine is a well-studied scaffold.[38,39] For the PFSA binder, no bulk dry-powder price is available; therefore, we estimate a cost based on the commercial price of Nafion membranes.[40] Using a Nafion membrane price of \$ 561 m^{-2}, a PFSA density of 2.0 g cm^{-3}, and a membrane thickness of 125 μm, we calculate an equivalent PFSA material cost of \$2,224 kg^{-1}. Based on industrial reports indicating that carbon nanotube costs span tens to hundreds of dollars 1195 per kilogram, a representative value of ~\$400 kg^{-1} was adopted; much lower-cost alternatives such 1196 as activated carbon (~\$2 kg^{-1}) may further reduce material costs.

Table S7. Cost per mass of $Na_4Fe(CN)_6$ and PCET electrode components

Component	**Cost ($ kg^{-1})**
$Na_4Fe(CN)_6$	1.785

Phenazine	10
PFSA	2,224
Carbon Nanotube (multi-walled)	400

The total concentration of $Na_4Fe(CN)_6$ is chosen to provide three times the capacity of the PCET-active electrode.

Table S8 outlines the assumed cost per area and lifetime of electrochemical cell components. The areal cost for graphite felt is derived from Zheng et al.[40] A cation exchange membrane is used for this analysis. A membrane cost of \$12 m^{-2} is assumed for sulfonated PEEK (SPEEK), based on analysis by Yuan *et al*.[41]

Table S8. Cost per area and lifetime of flow cell components.

Component	Cost per area (\$ m^{-2})	Lifetime (years)
Cation Exchange Membrane	12	2
Graphite Felt	16	5

We also consider replacing the cation-exchange membrane and graphite-felt counter electrode with a Na^+-intercalating solid electrode paired with a porous separator, which offers a potential route to reduce both capital and maintenance costs by eliminating the need for an ion-exchange membrane. In this configuration, the counter electrode functions as a reversible Na^+ reservoir, maintaining charge balance with the working electrode by intercalating Na^+ ions from seawater. The ion-selective membrane is substituted with a porous separator that prevents electrical short-circuiting while allowing ionic transport. A layered $NaMnO_2$ (NMO) electrode, with a specific capacity of 576 C g^{-1} and a composition of 90 wt% active material, 5 wt% binder, and 5 wt% conductive carbon, was used to determine the electrode's cost per gram.[42] Table S9 displays the cost and lifetime for each of these alternatives.[43] The lifetimes of the separator and electrode are assumed to be 10 years and 5 years, respectively. A cost factor of 1.4 was applied to all components above.

Table S9. Cost per area and lifetime of separator and sodium-intercalating electrode.

Component	Cost	Lifetime (years)
Separator (\$ m^{-2})	1.2	10

Sodium-Intercalating Electrode ($ kg^{-1})	14.3	5

Table S10 provides the capital costs of the membrane contactor and other balance-of-plant components required to separate CO_2 at a scale of 100,000 tons per year. The components included in this analysis are the hollow fiber membrane contactor (HFMC), water condenser, vacuum pump, and vacuum pump chiller. The HFMC is assumed to have a lifetime of 5 years whereas the other three components are assumed to have a lifetime of 10 years each. The price of the HFMC, water condenser, vacuum pump, and vacuum pump chiller are taken from a study by Digdaya et al.[4]

Table S10. Capital costs of membrane contactor components

Capital Costs (Membrane Contactor)	**Lifetime**	**Price ($)**
Hollow Fiber Membrane Contactor	5	16,410,652
Water Condenser	10	392,906
Vacuum Pump	10	6,635,118
Vacuum Pump Chiller	10	782,393

Levelized Cost

The capital charge factor (CCF, Equation (S30) is used to determine the fraction of the total initial (i.e., overnight) capital cost that must be expended per pay period. It is a function of the interest rate for discounting, r, and lifetime of the project, ŋ (in years):

$$CCF = \frac{r(1+r)^{\eta}}{(1+r)^{\eta} - 1} \tag{S30}$$

The levelized cost of CO_2 removal (LCCR), given in $ ton^{-1} of CO_2, is:

$$LCCR = \frac{OpEx + (CCF \times CapEx)}{CO_2\ removed\ per\ annum} \tag{S31}$$

where OpEx and CapEx are the operating expense per ton of CO_2 removed and overnight cost for the project, respectively.

Supplementary Fig.12a shows the breakdown of capital costs (total $ 13.15 ton CO_2^{-1}) for carbon removal based on the assumptions above for η = 25 years, evaluated at an operating current density of 10 mA cm^{-2}. This operating point lies near the optimal region identified in the model sweep, where the energetic cost and separation rate are both favorable. Pump-related costs are excluded,

consistent with scenarios in which the carbon capture unit is co-located with a desalination facility or a seawater-cooled power plant.

Operating Costs

Operating expenses considered in this analysis include the electricity required to run the electrochemical cell, the vacuum pump and its cooling, the removal of O_2 and N_2 from seawater before it is treated, and the cost of O&M, labor, and property taxes and insurance.

Operating expenses (S32) are related to the energetic cost of carbon removal from reversible seawater acidification ($P_{removal}$) and the energy inputs for the vacuum pump for CO_2 stripping (P_{str}), degasification of O_2 and N_2 (P_{dg}), and cooling of the vacuum pump ($P_{cooling}$), all in kWh ton_{CO2}^{-1} multiplied by the cost of commercial electricity (P_E), added to levelized annual cost of O&M and labor ($P_{O\&M,\ labor}$), and property taxes and insurance (P_{taxes}), all in \$ ton_{CO2}^{-1}. P_{str}, P_{dg}, $P_{cooling}$, $P_{O\&M,\ labor}$ and P_{taxes} are adopted from Digdaya *et* al.[4]

$$OpEx = P_E \times \left[P_{removal} + P_{str} + P_{dg} + P_{cooling}\right] + P_{O\&M,labor} + P_{taxes} \qquad \text{(S32)}$$

Table S11. Energy Consumption by Process Stage in Electrochemical Carbon Removal

Operating Expense Description	**kWh kg^{-1} CO_2**
Electrochemical Seawater Treatment	Parameter-Dependent
Vacuum Pump and Stripping	0.059
Degasification	0.014
Cooling	0.002

Direct operating costs are defined as the initial capital expenditure associated with the purchase and installation of all equipment, excluding future replacement costs. Indirect costs account for component-specific cost factors. The engineering, procurement, and construction (EPC) cost is calculated as the sum of direct and indirect costs. A contingency allowance equal to 10% of the EPC cost and an owner's cost equal to 5% of the EPC cost are then applied. The total overnight cost (TOC) is obtained as the sum of the EPC cost, contingency, and owner's cost.

The cost of O&M and labor is assumed to be 3.12% of the TOC. We assume the cost of property taxes, and insurance are assumed to be 2% of the TOC per year.

Sensitivity Analysis for Levelized Cost of CO_2 Removal

We varied current density while cell resistance and electrode capacity were kept constant at 5 Ω cm^2 and 1.54 C cm^{-2} per each cell, respectively. All area-specific values reported here are referenced to the geometric electrode area.

The relationship between current density and cost is roughly U-shaped, with the minimum cost occurring around 10 mA cm^{-2} (Supplementary Fig.12b). This trend results from capital and operating costs having opposite relationships with current density: capital cost decreases with increasing current density, whereas operating expenses increase with current density due to progressively higher electricity costs.

The lowest cost of CO_2 achievable for the above range of parameters is $ 21.4 ton CO_2^{-1}. A slightly lower cost ($18.1 ton CO_2^{-1}) is possible if the cation exchange membrane and graphite felt are replaced with a low-cost separator and sodium-intercalating electrode, respectively, based on the price and lifetime assumptions in Table S9. Table S12 compares the levelized cost between the two systems. We then constructed the levelized cost curve using experimentally measured energy input and separation rate data from **Error! Reference source not found.**a–b to provide a realistic assessment of system performance across current densities. As shown in Supplementary Fig.12c, the lowest levelized cost of CO_2 is $ 57.7 ton CO_2^{-1}, achieved at a current density of 1.2 mA cm^{-2}.

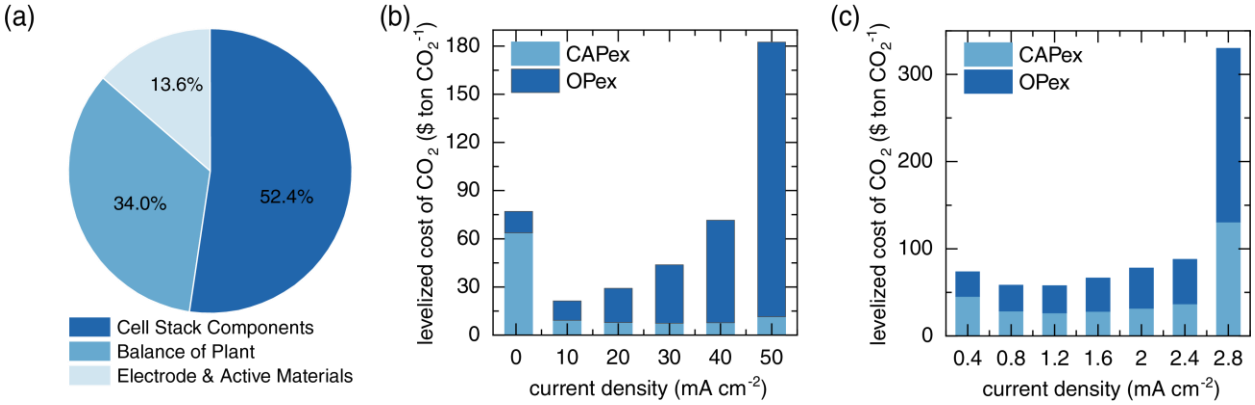

Supplementary Fig.12. Levelized cost analysis of the electrochemical carbon capture system. (a) Breakdown of levelized capital costs across major system components, including cell stack components, balance of plant, and electrode and active materials. (b) Total levelized cost of CO_2 ($ ton^{-1} CO_2), decomposed into CapEx and OpEx contributions as a function of current density (0.5–50 mA cm^{-2}), predicted from the techno-economic model with cell resistance and electrode capacity fixed at 5 Ω cm^2 and 1.54 C cm^{-2}, respectively. (c) Total levelized cost of CO_2 ($ ton^{-1} CO_2) as a function of current density based on experimentally measured energetic cost and separation rate (Fig.5), with CapEx and OpEx contributions shown separately.

Table S12. Levelized costs for the $Na_4Fe(CN)_6$ system and the intercalated electrode system.

System	Levelized CapEx ($ ton CO_2^{-1})	Levelized OpEx ($ ton CO_2^{-1})	Total Levelized Cost of CO_2 ($ ton CO_2^{-1})
Sodium Ferrocyanide Electrolyte + Ion-Exchange Membrane	9.2	12.2	21.4
Sodium-Intercalating Electrode + Separator	6.2	11.9	18.1

References

1 Aliaskari, M., Wezstein, J., Saravia, F. & Horn, H. A systematic analysis of operating parameters for CO2 capture from seawater by Bipolar Membrane Electrodialysis (BPMED). *Separation and Purification Technology* **339**, 126679 (2024). https://doi.org/https://doi.org/10.1016/j.seppur.2024.126679

2 Sharifian, R., Boer, L., Wagterveld, R. M. & Vermaas, D. A. Oceanic carbon capture through electrochemically induced in situ carbonate mineralization using bipolar membrane. *Chemical Engineering Journal* **438**, 135326 (2022). https://doi.org/https://doi.org/10.1016/j.cej.2022.135326

3 Eisaman, M. D. *et al.* CO2 extraction from seawater using bipolar membrane electrodialysis. *Energy & Environmental Science* **5**, 7346–7352 (2012). https://doi.org/10.1039/C2EE03393C

4 Digdaya, I. A. *et al.* A direct coupled electrochemical system for capture and conversion of CO2 from oceanwater. *Nature Communications* **11**, 4412 (2020). https://doi.org/10.1038/s41467-020-18232-y

5 Silcox, R., Villavicencio, F., Kipnis, T. & Bala Chandran, R. Effective Precipitate Cleaning with Reversible Flow Cell Sustains Stable Energy Intensity for Oceanic CO2 Removal. *ChemRxiv* **2026** https://doi.org/10.26434/chemrxiv-2026-b66r3

6 Kim, S. *et al.* Asymmetric chloride-mediated electrochemical process for CO2 removal from oceanwater. *Energy & Environmental Science*, 2030 – 2044 (2023). https://doi.org/10.1039/D2EE03804H

7 Yan, L., Bao, J., Shao, Y. & Wang, W. An Electrochemical Hydrogen-Looping System for Low-Cost CO2 Capture from Seawater. *ACS Energy Letters* **7**, 1947–1952 (2022). https://doi.org/10.1021/acsenergylett.2c00396

8 Yao, Z.-F., Wang, J.-Y. & Pei, J. Controlling morphology and microstructure of conjugated polymers via solution-state aggregation. *Progress in Polymer Science* **136**, 101626 (2023). https://doi.org/https://doi.org/10.1016/j.progpolymsci.2022.101626

9 Fischer, F. S. U. *et al.* Influence of Processing Solvents on Optical Properties and Morphology of a Semicrystalline Low Bandgap Polymer in the Neutral and Charged States. *Macromolecules* **46**, 4924–4931 (2013). https://doi.org/10.1021/ma400939z

10 *Polymer data handbook*. (Oxford University Press, 1999).

11 Parra-Puerto, A., Rubio-Garcia, J., Markiewicz, M., Zheng, Z. & Kucernak, A. Carbon Aerogel Based Thin Electrodes for Zero-Gap all Vanadium Redox Flow Batteries – Quantifying the Factors Leading to Optimum Performance. *ChemElectroChem* **9**, e202101617 (2022). https://doi.org/https://doi.org/10.1002/celc.202101617

12 Xie, X. & Holze, R. Electrode Kinetic Data: Geometric vs. Real Surface Area. *Batteries* **8**, 146 (2022).

13 Sayer, R. A., Hodson, S. L. & Fisher, T. S. Improved Efficiency of Dye-Sensitized Solar Cells Using a Vertically Aligned Carbon Nanotube Counter Electrode. *Journal of Solar Energy Engineering* **132** (2010). https://doi.org/10.1115/1.4001148

14 Pham, K.-C., McPhail, D. S., Wee, A. T. S. & Chua, D. H. C. Amorphous molybdenum sulfide on graphene–carbon nanotube hybrids as supercapacitor electrode materials. *RSC Advances* **7**, 6856–6864 (2017). https://doi.org/10.1039/C6RA27901E

15 Favero, G., Fusco, G., Mazzei, F., Tasca, F. & Antiochia, R. Electrochemical Characterization of Graphene and MWCNT Screen-Printed Electrodes Modified with AuNPs for Laccase Biosensor Development.

16 Sekretaryova, A. N., Vagin, M. Y., Volkov, A. V., Zozoulenko, I. V. & Eriksson, M. Evaluation of the Electrochemically Active Surface Area of Microelectrodes by Capacitive and Faradaic Currents. *ChemElectroChem* **6**, 4411–4417 (2019). https://doi.org/https://doi.org/10.1002/celc.201900989

17 Cao, Q., Hensley, D. K., Lavrik, N. V. & Venton, B. J. Carbon nanospikes have better electrochemical properties than carbon nanotubes due to greater surface roughness and defect sites. *Carbon* **155**, 250–257 (2019). https://doi.org/https://doi.org/10.1016/j.carbon.2019.08.064

18 Ryu, J. H. *et al.* All-Carbon Electrode Consisting of Carbon Nanotubes on Graphite Foil for Flexible Electrochemical Applications.

19 Gupta, A. *et al.* Nanostructured Polyaniline/Graphene/Fe2O3 Composites Hydrogel as a High-Performance Flexible Supercapacitor Electrode Material. *ACS Applied Energy Materials* **3**, 6434–6446 (2020). https://doi.org/10.1021/acsaem.0c00684

20 Kawai, T., Oyaizu, K. & Nishide, H. High-Density and Robust Charge Storage with Poly(anthraquinone-substituted norbornene) for Organic Electrode-Active Materials in Polymer–Air Secondary Batteries. *Macromolecules* **48**, 2429–2434 (2015). https://doi.org/10.1021/ma502396r

21 Kim, Y. S., Balland, V., Limoges, B. & Costentin, C. Cyclic voltammetry modeling of proton transport effects on redox charge storage in conductive materials: application to a TiO2 mesoporous film. *Physical Chemistry Chemical Physics* **19**, 17944–17951 (2017). https://doi.org/10.1039/C7CP02810E

22 Holzapfel, N. P., Augustyn, V. & Balland, V. Fundamentals of Proton-Insertion Coupled Electron Transfer (PICET) in Metal Oxides for Aqueous Batteries. *ACS Energy Letters* **10**, 1143–1164 (2025). https://doi.org/10.1021/acsenergylett.4c03076

23 Oka, K. *et al.* Poly(dihydroxybenzoquinone): its high-density and robust charge storage capability in rechargeable acidic polymer–air batteries. *Chemical Communications* **56**, 4055–4058 (2020). https://doi.org/10.1039/D0CC00660B

24 Oka, K., Murao, S., Kataoka, M., Nishide, H. & Oyaizu, K. Hydrophilic Anthraquinone-Substituted Polymer: Its Environmentally Friendly Preparation and Efficient Charge/Proton-Storage Capability for Polymer–Air Secondary Batteries. *Macromolecules* (2021). https://doi.org/10.1021/acs.macromol.1c00865

25 Oka, K., Murao, S., Kobayashi, K., Nishide, H. & Oyaizu, K. Charge- and Proton-Storage Capability of Naphthoquinone-Substituted Poly(allylamine) as Electrode-Active Material for Polymer–Air Secondary Batteries. *ACS Applied Energy Materials* (2020). https://doi.org/10.1021/acsaem.0c02178

26 Sterby, M. *et al.* Characterization of PEDOT-Quinone Conducting Redox Polymers for Water Based Secondary Batteries. *Electrochimica Acta* **235**, 356–364 (2017). https://doi.org/https://doi.org/10.1016/j.electacta.2017.03.068

27 Sieuw, L., Ernould, B., Gohy, J.-F. & Vlad, A. On the improved electrochemistry of hybrid conducting-redox polymer electrodes. *Scientific Reports* **7**, 4847 (2017). https://doi.org/10.1038/s41598-017-05063-z

28 Lin, Z. *et al.* A high capacity small molecule quinone cathode for rechargeable aqueous zinc-organic batteries. *Nature Communications* **12**, 4424 (2021). https://doi.org/10.1038/s41467-021-24701-9

29 Savéant, J.-M. & Costentin, C. *Elements of Molecular and Biomolecular Electrochemistry: An Electrochemical Approach to Electron Transfer Chemistry*. 2 edn, (Wiley, 2022).

30 Lewis, N. B., Bisbey, R. P., Westendorff, K. S., Soudackov, A. V. & Surendranath, Y. A molecular-level mechanistic framework for interfacial proton-coupled electron transfer kinetics. *Nature Chemistry* **16**, 343–352 (2024). https://doi.org/10.1038/s41557-023-01400-0

31 Abhayawardhana, A. D. & Sutherland, T. C. Heterogeneous proton-coupled electron transfer of a hydroxy-anthraquinone self-assembled monolayer. *Journal of Electroanalytical Chemistry* **653**, 50–55 (2011). https://doi.org/https://doi.org/10.1016/j.jelechem.2011.01.009

32 Zeebe, R. E. & Wolf-Gladrow, D. *CO2 in Seawater: Equilibrium, Kinetics, Isotopes*. (Elsevier, 2005).

33 Dickson, A. G. & Goyet, C. Handbook of methods for the analysis of the various parameters of the carbon dioxide system in sea water. Version 2. (United States, 1994).

34 Guyer, J. E., Wheeler, D. & Warren, J. A. FiPy: Partial Differential Equations with Python. *Computing in Science & Engineering* **11**, 6–15 (2009). https://doi.org/10.1109/MCSE.2009.52

35 Zhang, W., Ozden, A., Yang, Y., Xu, A. & Li, F. Hidden Acidification Challenges in Electrochemical Ocean Decarbonization. *ACS Energy Letters* **10**, 2788–2792 (2025). https://doi.org/10.1021/acsenergylett.5c00900

36 Morel, F. M. M. & Hering, J. G. *Principles and Applications of Aquatic Chemistry*. (John Wiley & Sons, 1993).

37 Ross, B., Haussener, S. & Brinkert, K. Impact of Gas Bubble Evolution Dynamics on Electrochemical Reaction Overpotentials in Water Electrolyser Systems. *The Journal of Physical Chemistry C* **129**, 4383–4397 (2025). https://doi.org/10.1021/acs.jpcc.5c00220

38 Gregory, T. D., Perry, M. L. & Albertus, P. Cost and price projections of synthetic active materials for redox flow batteries. *Journal of Power Sources* **499**, 229965 (2021). https://doi.org/https://doi.org/10.1016/j.jpowsour.2021.229965

39 Emmel, D. *et al.* Benchmarking organic active materials for aqueous redox flow batteries in terms of lifetime and cost. *Nature Communications* **14**, 6672 (2023). https://doi.org/10.1038/s41467-023-42450-9

40 Zheng, M., Sun, J., Meinrenken, C. & Wang, T. Pathways Toward Enhanced Techno-Economic Performance of Flow Battery Systems in Energy System Applications. *Journal of Electrochemical Energy Conversion and Storage* **16** (2018). https://doi.org/10.1115/1.4040921

41 Yuan, Z. *et al.* Low-cost hydrocarbon membrane enables commercial-scale flow batteries for long-duration energy storage. *Joule* **6**, 884–905 (2022). https://doi.org/https://doi.org/10.1016/j.joule.2022.02.016

42 Vaalma, C., Buchholz, D., Weil, M. & Passerini, S. A cost and resource analysis of sodium-ion batteries. *Nature Reviews Materials* **3**, 18013 (2018). https://doi.org/10.1038/natrevmats.2018.13

43 Castro, M., Domalanta, M. R., Rosario, J. & Ocon, J. Energy, power, and cost optimization of a sodium-ion battery pack via a combined physics-based and cost modeling approach. *Journal of Energy Storage* **94**, 112414 (2024). https://doi.org/10.1016/j.est.2024.112414